

Analysis of Preferential Nucleation Sites for Austenite in Deformed Ferrite-pearlite Structure by Experimental and Computational Approaches

Shohei YABU*
Toshinobu NISHIBATA

Koutarou HAYASHI

Abstract

To clarify what serves as the priority site for austenite nucleation, microstructure evolution during continuous heating was experimentally studied using specimen sheets of the deformed ferrite-pearlite structure of an Fe-0.1 mass% C-2.0 mass% Mn alloy. At 998 K, while 97% of austenite grains were found to nucleate at high-angle boundaries between ferrite grains, no austenite nucleation was observed inside ferrite grains. At 1 028 K, on the other hand, austenite nucleation was found to occur inside ferrite grains. According to thermodynamic calculation, austenite nucleation requires cementite at 1 032 K or lower, which indicates that cementite on high-angle boundaries between ferrite grains serves as the priority site for austenite nucleation. The above test result agrees well with the calculation results based on nucleation theories.

1. Introduction

The automotive industry is making efforts to reduce car weight and enhance collision safety. The use of high-strength steel for the bodies is an important measure to achieve both of these aims simultaneously. Ultra-high-strength steel with a tensile strength of 980 MPa or more is used especially for the frame structural members.¹⁾

In the manufacture of such frame structural members, good formability is required of the steel in addition to high strength. The formability of steel sheets is evaluated widely in terms of elongation at the tensile test, which, however, tends to lower as the tensile strength increases,²⁾ and it is not easy to produce steel having both high strength and good formability.

As the breakthrough to solve this problem, steel sheet products of high strength and high formability have been developed taking advantage of dual-phase (DP) steel, low-alloy TRIP (transformation induced plasticity) steel, etc. These types of steel have a composite structure comprising ferrite as the main phase. The DP steel have a structure in which martensite is scattered in a matrix of ferrite, wherein the martensite affects both strength and elongation. In the low-alloy TRIP steel, on the other hand, the structure contains aus-

tenite, or what is known as retained austenite, in addition to martensite, and the austenite markedly improves elongation thanks to its TRIP effect.³⁾ Therefore, to obtain high strength and good formability with composite-structure steel, it is essential to control the formation of martensite and retained austenite.

In most cases, high-strength steel sheets are produced through hot rolling, cold rolling, and then continuous annealing,⁴⁾ and their metallographic structure is controlled as intended through this sequence of processes. Here, the steel after hot rolling usually has a ferrite-pearlite structure,⁵⁾ then austenite forms through cold rolling and heating (during the annealing) to above the A_c1 transformation point,⁶⁻¹¹⁾ and the austenite thus formed is transformed into martensite or retained austenite during cooling in the continuous annealing process.⁶⁾ It is therefore important to clarify the structural change from the ferrite-pearlite structure after cold rolling, especially the austenitic transformation during the heating for annealing. The ferrite-pearlite structure after cold rolling is hereinafter referred to as the deformed ferrite-pearlite structure.

When this deformed ferrite-pearlite structure is heated, austenite forms, in addition, ferrite recrystallizes, and cementite in pearlite is

* Sheet & Coil Research Lab., Steel Research Laboratories
20-1 Shintomi, Futtsu City, Chiba Pref. 293-8511

spheroidized.⁷⁾ It has been reported that not only the ferrite recrystallization but also the austenitic nucleation and growth are influenced by the rate of the heating.⁸⁾ In fact, there is a report stating that when the deformed ferrite-pearlite structure of an Fe-0.17 mass% C-0.74 mass% Mn alloy is heated, the number of austenitic nucleation sites increases with the higher heating rate, and the austenitic transformation is accelerated.⁹⁾ The number of nucleation sites changes depending on strain energy, the distribution of cementite, the number of ferrite grain boundaries, etc., but which of these is the most significant governing factor was unclear.

Against this background, we aimed at clarifying what served as the preferential nucleation sites for austenite during continuous annealing by tests using the deformed ferrite-pearlite structure of an Fe-0.1 mass% C-2.0 mass% Mn alloy as the specimen. We also studied the factors influencing austenite nucleation and tried to clarify what served as the priority nucleation sites through calculation based on classical nucleation theories. The present paper reports the results of these studies.

2. Body

2.1 Test method

An Fe-0.1 mass% C-2.0 mass% Mn alloy was melted in a vacuum furnace and cast into 50 kg ingots. After hot rolling the ingots, the rolled sheets were additionally held at 873 K for 1 h, air cooled to room temperature, and then scale was removed from both surfaces by grinding; the final sheet thickness was 2.5 mm. The hot-rolled sheets were cold rolled to a thickness of 1.2 mm, their thermal expansion (or dilatation) was measured by heating to 1 223 K at a rate of 28 K/s, and the relationship between the temperature and the coefficient of thermal expansion was calculated from the amount of dilatation. Then, the variation of thermal expansion per unit heating was defined by the following method: the gradient of the thermal expansion curve of the material at temperature T was approximated by fitting a straight line to the curve in the range from $T-5$ K to $T+5$ K, and defining the gradient of the straight line as the temperature-dependent variation of the thermal expansion curve at temperature T . In addition to the above, test pieces were prepared by heating the cold-rolled sheets to different temperatures from 985 to 1 028 K at a heating rate of 28 K/s, water cooling them, polishing them with alumina at a section surface, and etching the surface with nital.

The specimens were observed at the section through a scanning electron microscope (SEM). A specimen heated to 998 K was examined in terms of crystallinity (orderliness of atomic alignment) and grain boundaries by the method of electron back scattering diffraction pattern (EBSD), wherein the working distance (WD) was set at 10 mm, accelerating voltage at 15 kV, the distance between measurement points at 50 nm, and data were collected in an area of $50 \times 50 \mu\text{m}$. In addition, the carbon concentric distribution of the same specimen heated to 998 K was measured using a field emission electron probe micro analyzer (FE-EPMA), setting the distance between measurement points at 200 nm. The specimen sections were finished using colloidal silica before the EBSD and FE-EPMA examinations.

2.2 Test result

2.2.1 Microstructural change during continuous heating

The microstructures of the hot- and cold-rolled sheets are given, respectively, in parts (a) and (b) of Fig. 1; here, ND means the thickness (normal) direction, RD the rolling direction, F ferrite, and P pearlite (which applies also to other images hereinafter). In Fig. 1(a), there are areas of an even tone and others scattered with particles. The former is pro-eutectoid ferrite, and since the particles are

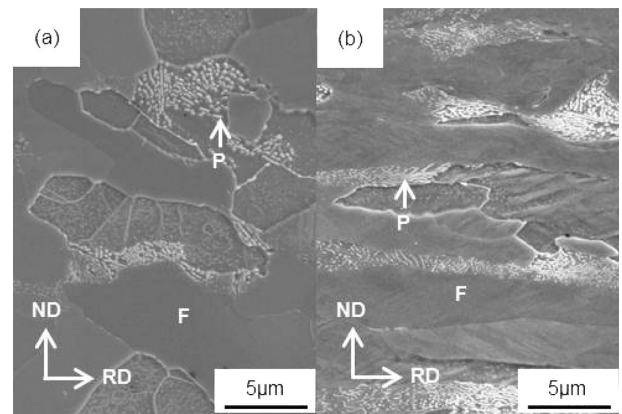


Fig. 1 Cross-sectional microstructures of (a) hot-rolled and (b) cold-rolled specimens of Fe 0.1 mass% C-2.0 mass% Mn alloy (F: ferrite, P: pearlite, ND: normal direction, RD: rolling direction)

cementite, the latter is pearlite. This indicates that a ferrite-pearlite structure was obtained by hot rolling an Fe-0.1 mass% C-2.0 mass% Mn alloy and holding it isothermally at 873 K. On the other hand, Fig. 1(b) shows that the ferrite-pearlite structure was elongated in the rolling direction, and there were shear zones in ferrite grains, indicating that the structure of the cold-rolled sheets is the deformed ferrite-pearlite structure.

The analysis result of the variation of thermal expansion per unit heating of the cold rolled sheet specimens during heating at a rate of 28 K/s is given in Fig. 2. In part (a), the ordinate represents thermal expansion, and the abscissa temperature. Figure 2(a) shows that the Ac_1 and Ac_3 temperatures of the material were 988 K and 1 110 K, respectively. In the graph, I is the temperature range below Ac_1 , and IV that over Ac_3 . Figure 2(b) shows the relationship between temperature and the variation of the dilatation. The graph seems to indicate that the austenitic transformation of the alloy during heating progresses in plural stages; according to Azizi et al., the change from the deformed ferrite-pearlite structure follows five steps.⁹⁾

According to the result of the present study, too, the austenitic transformation between I and IV can be divided into two parts. In the range II in Fig. 2(b), the thermal expansion per unit heating fell markedly, which presumably resulted from the nucleation and growth of austenite advancing in parallel together with the melting of cementite. Thereafter, in the range III, the variation of thermal expansion per unit heating continued to fall with the increase in temperature, and at 1 070 K it began to increase. This is presumably because cementite had disappeared and only the austenitic growth advanced.⁹⁾ Following the argument of Azizi et al.,⁹⁾ the boundary temperature between II and III is hereinafter referred to as Ac_θ . By the graph in Fig. 2(b), Ac_θ is 1 025 K. It follows, therefore, that austenitic nuclei are considered to form in the heating temperature range of 988 to 1 025 K.

Next, Fig. 3 shows the microstructures of specimens prepared by heating the cold-rolled sheets to different temperatures at a heating rate of 28 K/s and then water cooling them. In this figure and others hereinafter, C and M indicate spheroidal cementite and martensite, respectively. This martensite formed as follows: austenite formed during the heating, and it transformed into martensite during the water cooling. As seen in Fig. 3(a), the structure obtained at 985 K (immediately below Ac_1) contained recrystallized ferrite in the deformed ferrite-pearlite structure. In addition, spheroidal cementite

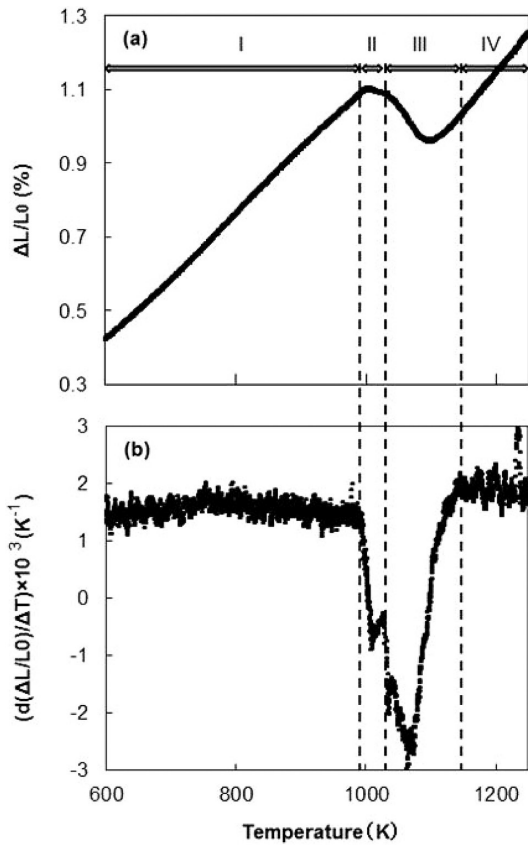


Fig. 2 (a) Dilatometry curve, (b) Temperature derivative of dilatation (heating rate: 28 K/s, specimens: cold-rolled sheet of Fe-0.1 mass% C-2.0 mass% Mn alloy)

was also found on the grain boundaries of ferrite, and part of the cementite in the pearlite was spheroidized.

Martensite was not found, which indicates that austenite did not form. On the other hand, as is shown in Fig. 3 (b), martensite was found in the structure obtained through heating the specimens to 998 K (immediately above A_{c1}), and as a consequence, from the results of the analysis in Fig. 2 as well as the microstructural observation, it was clarified that austenite nucleated in the range from 985 to 998 K during the heating. In addition, as indicated with the black arrows in Fig. 3 (b), austenite nucleated at the ferrite-pearlite interfaces, on ferrite grain boundaries and inside pearlite grains. It has to be noted here that austenite did not form in ferrite grains.

As seen in Fig. 3 (c), in the structure obtained by heating the specimens to 1028 K (immediately above A_{c0}), substantially all austenite was distributed in the rolling direction. Note here, however, that part of the austenite was found to form inside grains of recrystallized ferrite.

2.2.2 Priority nucleation sites for austenite

The structure of the specimen shown in Fig. 3 (b) was examined by the EBSD method. **Figures 4 (a) and (b)** are an image quality (IQ) map and a grain boundary map, respectively, of a specimen obtained by heating one of the steel sheets to 998 K and then water cooling it. The IQ value is an indicator of the distinctness of the Kikuchi lines, and it decreases depending on the strain field, or the flaw in crystallinity, resulting from lattice defects in the area to which the electron beam is irradiated. In the image of Fig. 4 (a), light areas represent zones of high crystallinity, and dark areas those of low crystallinity;

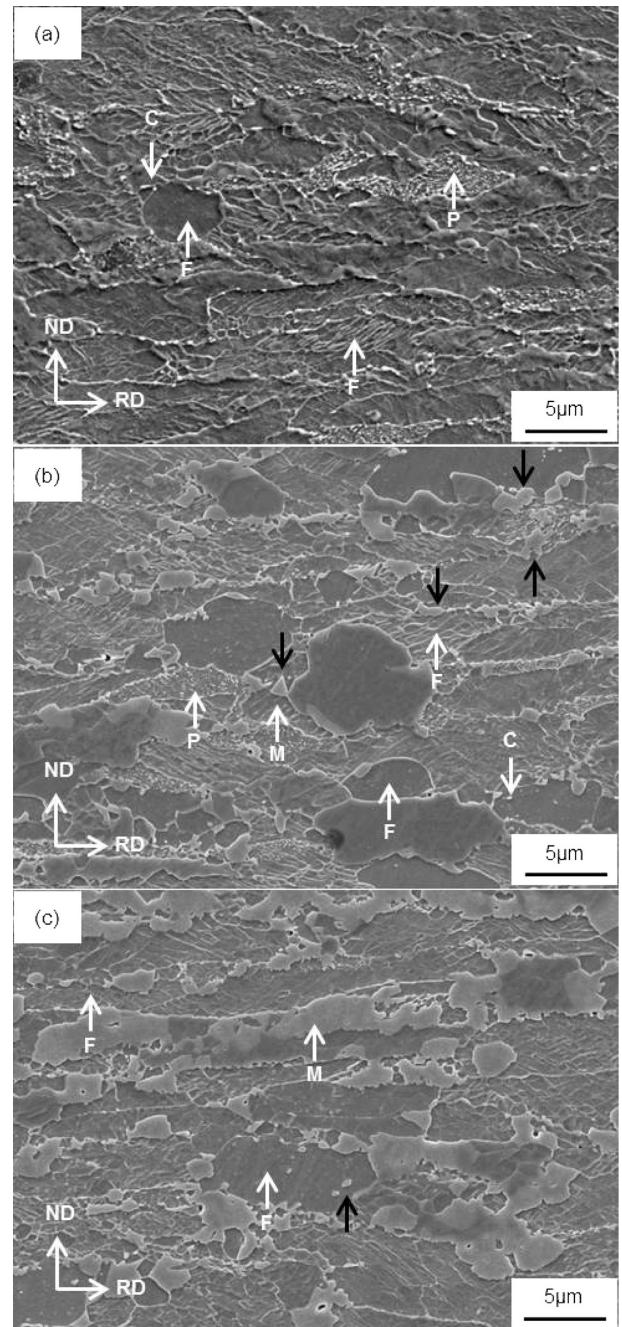


Fig. 3 Cross-sectional microstructures of cold-rolled sheets of Fe-0.1 mass% C-2.0 mass% Mn alloy heated at 28 K/s to (a) 985 K, (b) 998 K and (c) 1028 K (F: ferrite, P: pearlite, C: cementite, M: martensite, γ : austenite, ND: normal direction, RD: rolling direction)

martensite usually appears dark in IQ maps,^{12, 13)} recrystallized ferrite light in contrast, and deformed ferrite and deformed pearlite intermediate in the middle between the two. In the present analysis, the areas of an IQ value of 300 or less were judged to be martensite.

The image of Fig. 4 (b) was created by superimposing a martensite distribution map on a grain boundary map; the red curves show high-angle grain boundaries, and the blue curves low-angle grain boundaries. Here, the grain boundaries are classified as follows: when the difference θ in the crystal orientations of two adjacent

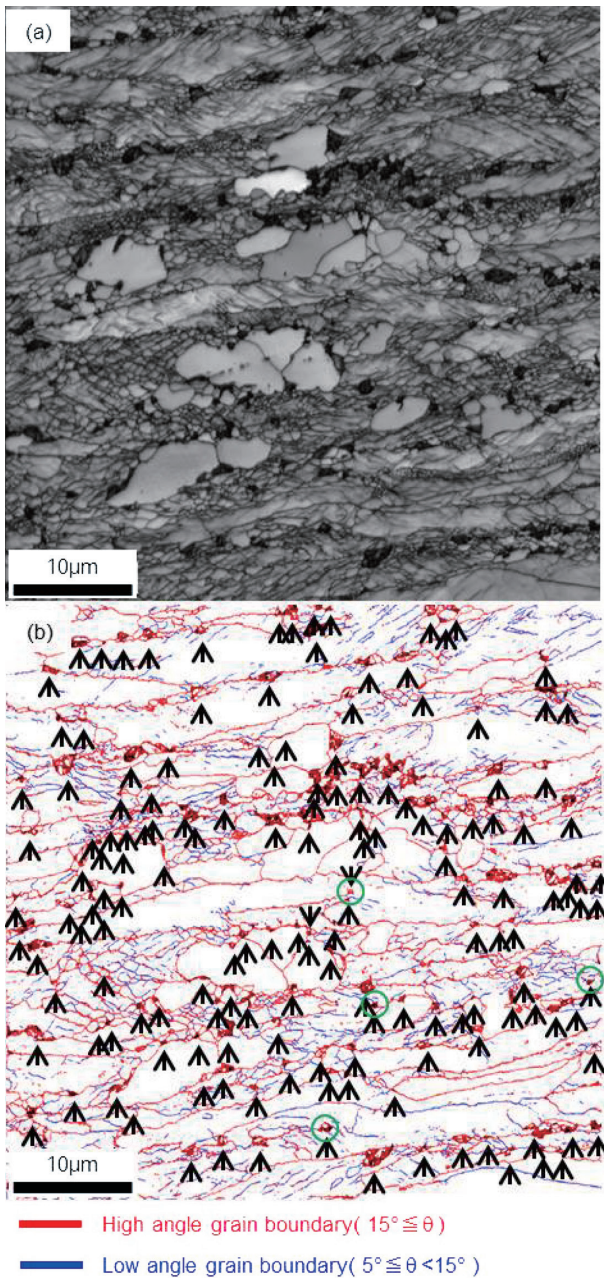


Fig. 4 EBSD analysis of cross-sectional structure of specimen sheet heated to 998 K
(a) Image quality map, (b) Grain boundary map

grains is 15° or more ($15^\circ \leq \theta$), the boundary between them is a high-angle boundary, and when θ is 5° or more and smaller than 15° ($5^\circ \leq \theta < 15^\circ$), the boundary is a low-angle boundary.¹⁴⁾ In the area of $2500 \mu\text{m}^2$, 158 martensite grains were counted. The black arrows in the map indicate martensite grains flanking on one or more high-angle boundaries, and the green circles mark those flanking on one or more low-angle boundaries in pearlite. Assuming that the martensite was austenite during the heating, the relationship between the austenite and the grain boundaries was analyzed, and as a result, 97% of the austenite grains were found to flank on one or more high-angle boundaries, and the remaining 3% on one or more low-angle boundaries in pearlite. This analysis result indicates that high-angle grain boundaries are the priority nucleation sites for aus-

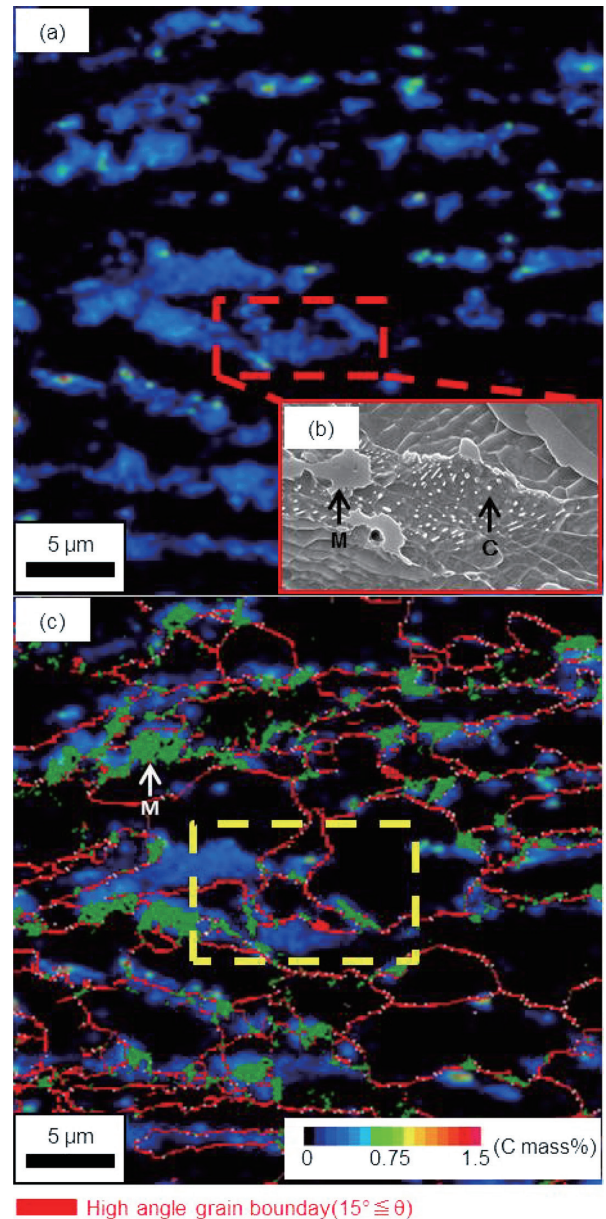


Fig. 5 FE-EPMA analysis of specimen sheet heated to 998 K
(a) Carbon concentration map, (b) SEM micrograph of area surrounded by red dotted lines, (c) Martensite structure and high-angle grain boundaries superimposed on (a)
(C: cementite, M: martensite)

tenite.

Then, the cold-rolled sheets were heated to 998 K at a rate of 28 K/s and then water cooled, and the sheets thus obtained were analyzed in terms of high-angle grain boundaries and the carbon concentration distribution near those boundaries using an FE-EPMA; the result is given in Fig. 5. The carbon concentration distribution given in part(a) shows that carbon concentration is high in the area surrounded by dotted red lines. Part(b) shows the microstructure of this area. Spheroidal cementite, which resulted from the cementite in pearlite having spheroidized during the heating, is seen to be scattered in a higher density there than in surrounding areas. In Fig. 5(c), the carbon concentration distribution given in part(a) is superimposed on the martensite and high-angle grain boundaries in the

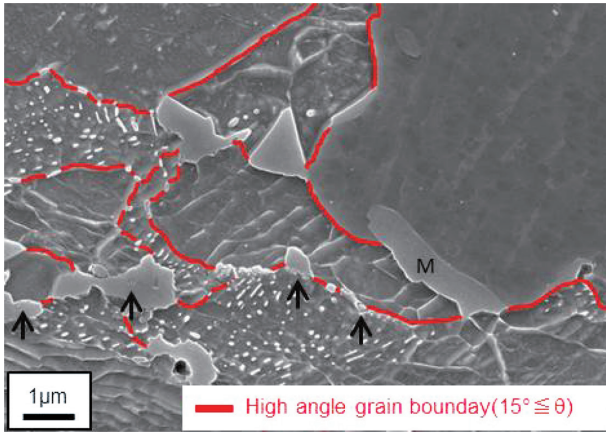


Fig. 6 Typical austenite structure of specimen heated to 998 K (M: martensite)

same area. Here, the green areas are martensite, and red curves show high-angle grain boundaries. The image demonstrates that martensite grains flanking on one or more high-angle boundaries are located near the areas where spheroidal cementite is in high concentration.

Figure 6 shows the microstructure in the framed area in Fig. 5(c); here the red curves are high-angle grain boundaries. As the black arrows indicate, some martensite grains flanking on one or more high-angle boundaries contained cementite inside them.

2.3 Discussion

2.3.1 Experimental study on preferential nucleation sites for austenite

Based on the test results presented above, we studied the factors influencing the nucleation of austenite. In the structure of the specimens heated to 998 K (immediately above A_{c1}), 97% of austenite grains flanked on one or more high-angle boundaries, and the remaining 3% on low-angle boundaries in pearlite. In addition, the former grains were found to form near areas where spheroidal cementite was in high concentration, which indicates that austenitic nucleation requires both cementite and high-angle grain boundaries of ferrite. With respect to the austenite grains flanking on low-angle boundaries in pearlite, on the other hand, it was surmised that the strain energy that existed before the heating had some influence over their formation, but the number of such austenite grains was small. Under the conditions of the present study, therefore, the influence of strain energy over the austenite nucleation is considered smaller than the influence of high-angle grain boundaries and cementite.

2.3.2 Analysis based on classical nucleation theories

We studied the influences of cementite and high-angle grain boundaries over the austenitic nucleation based on classical nucleation theories.^{15, 16)}

A study report states that, when austenite nucleates from a ferrite-cementite structure, the nuclei form on the ferrite side of the interfaces between ferrite and cementite.¹⁷⁾ In consideration of this, the cases of austenite nucleation at a ferrite-cementite interface are classified as follows: the case in which cementite is located at a high-angle boundary of two ferrite grains is Case I; another in which the cementite is located inside a ferrite grain is Case II; and yet another is Case III in which a boundary edge^{15, 18)} flanking on three ferrite grains serves as the site of austenitic nucleation. Figure 7 schematically shows Cases I, II, and III. Disregarding the effects of grain boundary energy and interface energy over the shape of austenite nuclei,^{15, 18)} the present analysis assumed that an austenite nucleus is hemispherical in Cases I and II, and it is spherical in Case

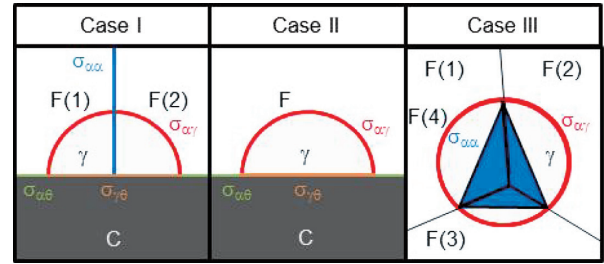


Fig. 7 Schematic illustration of austenite nucleation from ferrite and cementite

Case I: Austenite nucleating at ferrite grain boundary flanking on cementite

Case II: Austenite nucleating in ferrite grain flanking on cementite

Case III: Austenite nucleating at edges of ferrite grain boundaries (F: ferrite, C: cementite, γ : austenite, $\sigma_{\alpha\alpha}$: boundary between ferrite grains, $\sigma_{\alpha\gamma}$: ferrite/austenite interface, $\sigma_{\alpha\beta}$: ferrite/cementite interface, $\sigma_{\gamma\beta}$: austenite/cementite interface)

III.

According to classical nucleation theories, steady-state nucleation rate J_s^* is expressed as follows:¹⁹⁾

$$J_s^* = N_v \beta^* Z \exp\left(-\frac{\Delta G^*}{kT}\right) \quad (1)$$

Where N_v is the density of nucleation sites, β^* is the frequency factor, Z is the Zeldovich factor, k is the Boltzmann constant, and ΔG^* is the activation energy for nucleation. The values of ΔG^* were obtained for Cases I to III. The following equations express ΔG^* in Cases I, II, and III, respectively:

$$\Delta G^* = \frac{64\pi}{3(\Delta G_v)^2} \left(\frac{1}{2} \sigma_{\alpha\gamma} + \frac{1}{4} \sigma_{\gamma\beta} - \frac{1}{4} \sigma_{\alpha\beta} - \frac{1}{8} \sigma_{\alpha\alpha} \right)^3 \quad (2)$$

$$\Delta G^* = \frac{64\pi}{3(\Delta G_v)^2} \left(\frac{1}{2} \sigma_{\alpha\gamma} + \frac{1}{4} \sigma_{\gamma\beta} - \frac{1}{4} \sigma_{\alpha\beta} \right)^3 \quad (3)$$

$$\Delta G^* = \frac{16\pi}{3(\Delta G_v)^2} (\sigma_{\alpha\gamma} - 0.406\sigma_{\alpha\alpha})^3 \quad (4)$$

Here, the symbols are as follows: ΔG_v is the free energy change per unit volume resulting from the transformation of the deformed ferrite-pearlite structure into austenite, which is the driving force for austenitic nucleation; $\sigma_{\alpha\alpha}$ is the boundary energy between ferrite grains; $\sigma_{\alpha\gamma}$ is the interface energy between ferrite and austenite; $\sigma_{\alpha\beta}$ is that between ferrite and cementite; and $\sigma_{\gamma\beta}$ is that between austenite and cementite. The equilibrium concentrations of C and Mn in ferrite (to be explained later) and the value of ΔG_v were calculated using Thermo-Calc 2016 b (Thermodynamics Database TCFE8²⁰⁾).

The value of ΔG_v is different depending on the presence of cementite (Cases I and II) or its absence (Case III). In Cases I and II, ferrite and cementite are adjacent to each other, and for this reason, C and Mn are presumed to be easily distributed between the two structures during heating. Their distribution is supposed to follow orth-equilibrium in the present study, and in Case III, the concentrations of C and Mn in ferrite during heating, to be unchanged. Note that the specimen sheets were prepared by holding at 873 K for 1 h, as explained in Sub-section 2.1. Accordingly, the concentrations of C and Mn were supposed to be equal to their equilibrium concentrations on the ferrite side of the ferrite-cementite interface at 873 K; the concentrations of C and Mn are calculated at 0.0020 and 1.6 mass%, respectively.

Next, the assumptions for the present study under which austenite nucleates from ferrite in Cases I to III are explained. The first assumption is that C and Mn are distributed between the ferrite matrix

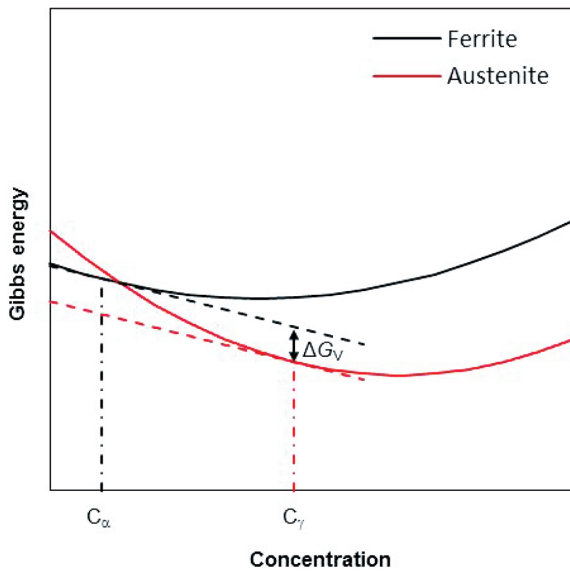


Fig. 8 Schematic illustration of driving force for austenite nucleation from ferrite matrix

and austenite nuclei. The second assumption is that the concentrations of C and Mn in austenite nuclei are determined such that the difference in the Gibbs energy between the ferrite matrix and the austenite nuclei is largest, or that the gradient of the Gibbs energy curve in the austenite nuclei is equal to the same in the ferrite phase, as by the parallel tangent rule;²¹⁻²³ ΔG_v is the difference in the Gibbs energy. **Figure 8** is a schematic representation of the case in which austenite nucleates from the ferrite matrix. Here, the ordinate represents the Gibbs energy, and the abscissa the solute concentration, the black curve is for ferrite and the red curve for austenite, and the solute concentration in ferrite is c_{α} , and that in austenite nuclei c_{γ} .

The grain boundary energy of ferrite was set at $\sigma_{aa} = 0.77 \text{ J/m}^2$,²⁴ the interface energy between ferrite and austenite at $\sigma_{\alpha\gamma} = 0.72 \text{ J/m}^2$, the same between ferrite and cementite at $\sigma_{\alpha\theta} = 0.71 \text{ J/m}^2$, and that between austenite and cementite at $\sigma_{\gamma\theta} = 0.67 \text{ J/m}^2$.^{25,26}

2.3.3 Analysis result of preferential nucleation sites for austenite

Figure 9 shows the calculation results of ΔG_v (the driving force for austenitic nucleation) in Cases I, II, and III; the ordinate represents the absolute value of ΔG_v , the abscissa the temperature, the solid line corresponds to Cases I and II, and the dotted line to Case III. Ferrite, austenite, and cementite are in an equilibrium at 927 K or above and austenitic nucleation can occur in Cases I and II. In Case III, on the other hand, ΔG_v becomes negative and austenitic nucleation can occur at 1032 K or above. The graph shows that the absolute value of ΔG_v is larger in Cases I and II than in Case III at any temperature. This means that when C and Mn are distributed between ferrite and cementite, the nucleation driving force increases on the ferrite side of the interface between the two, and austenitic nucleation is accelerated.

Figure 10 shows ΔG^* , the activation energy for austenitic nucleation, in Cases I and II; the ordinate represents ΔG^* , the abscissa the temperature, the circles the calculation results for Case I, and the triangles those for Case II. The graph shows that ΔG^* decreases with higher temperature in both Cases I and II, and the value of ΔG^* of Case I is less than a half that of Case II at any temperature. Note that in Case I ΔG^* is $1.3 \times 10^{-14} \text{ J}$ at 1110 K (A_{c3}), which indicates that cementite on high-angle grain boundaries serves as the preferential nucleation sites for austenite. Moreover, cementite increases the

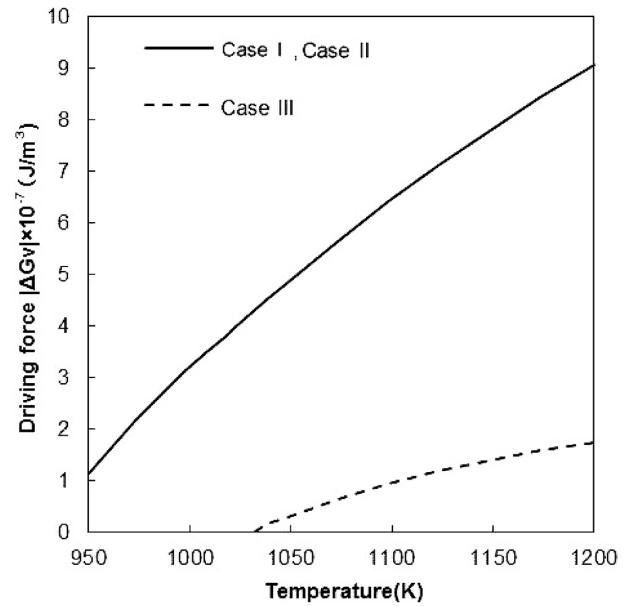


Fig. 9 Relationship between driving force for austenite nucleation and temperature (Fe-0.1 mass% C-2.0 mass% Mn alloy)

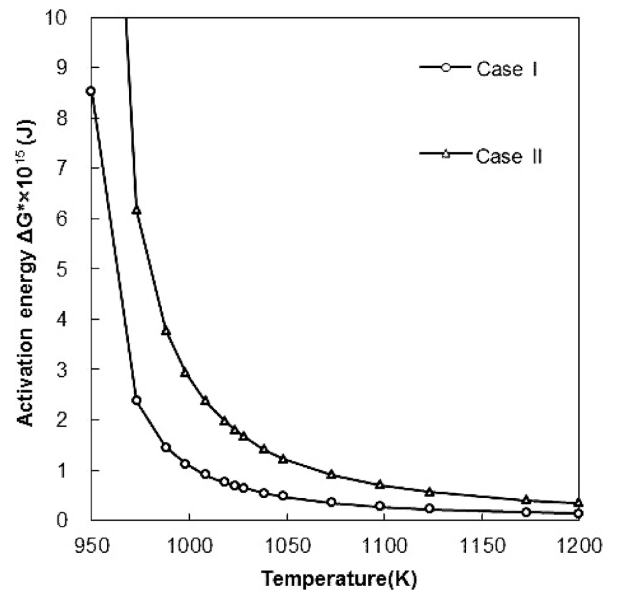


Fig. 10 Relationship between activation energy for austenite nucleation and temperature (Fe-0.1 mass% C-2.0 mass% Mn alloy)

driving force for austenite nucleation, and high-angle grain boundaries of ferrite decrease the driving force. This means that preferential nucleation sites for austenite are influenced by both cementite and high-angle grain boundaries.

The reason why ΔG^* is smaller in Case I than in Case II is presumably as follows: when austenite nucleates in Case I, the grain boundary between ferrite grains F(1) and F(2) shown in Fig. 7 disappears, and as a result, the decrease in free energy due to the nucleation is greater in Case I than in Case II. When a ferrite-ferrite grain boundary and a ferrite-cementite interface meet to form an edge as in Case I, austenite nucleates more easily. The calculation result

shown in Fig. 10 explains the structural observation of Fig. 6, and cementite inside austenite grains is presumed to be located at high-angle grain boundaries of ferrite.

As stated earlier, austenite nucleated at 998 K and the nucleation sites were principally the high-angle grain boundaries of ferrite. This type of nucleation is classified as Case I. On the other hand, the austenite that formed inside ferrite grains of the specimens heated to 1028 K is considered to result from the nucleation of Case II, because, according to the equilibrium calculation, ΔG_v is 0 in Case III. From Fig. 9, the value of ΔG^* at 998 K is 1.5×10^{-15} J in Case I, and 3.9×10^{-15} J in Case II. When the temperature rises from 998 to 1028 K, the value of ΔG^* of Case II falls to 1.7×10^{-15} J, very close to that in Case I at 998 K. As the above shows, the austenitic nucleation temperature of an Fe-0.1 mass% C-2.0 mass% Mn alloy falls by 30 K owing to the nucleation acceleration effect of high-angle grain boundaries. It has thus been clarified that theoretical analysis of austenitic nucleation by calculation provides a good explanation of the results obtained through tests.

3. Conclusion

To clarify what serves as the preferential nucleation sites for austenite, we investigated the structural evolution processes during continuous heating using specimens of the deformed ferrite-pearlite structure of an Fe-0.1 mass% C-2.0 mass% Mn alloy. At 998 K, 97% of the austenite grains formed at high-angle grain boundaries of ferrite, the remaining 3% at low-angle grain boundaries in pearlite, and austenite did not form inside ferrite grains. At 1028 K, in contrast, austenite was found to have newly formed inside ferrite grains. Thermodynamic calculation deems that austenitic nucleation at 1032 K or below requires cementite. This means that cementite at the high-angle grain boundaries serves as the preferential nucleation sites for austenite.

According to calculations based on classical nucleation theory, when cementite is located at high-angle grain boundaries of ferrite, the activation energy for austenitic nucleation at 998 K is 1.5×10^{-15} J. When it is located inside a ferrite grain, on the other hand, the ac-

tivation energy is 3.9×10^{-15} J. High-angle grain boundaries of ferrite, therefore, decrease the activation energy for austenitic nucleation, and thus accelerate the nucleation. In addition, according to a calculation regarding the specimen alloy, the effect of the high-angle grain boundaries of ferrite to accelerate austenitic nucleation lowers the austenitic nucleation temperature by 30 K, which agrees with the experimental observation.

References

- 1) Takahashi, M. et al.: Shinnittetsu Giho. (391), 27 (2011)
- 2) Edited by Joint Study Committee on Automobile Body Materials: High-tensile Strength Steel Handbook. ISIJ, 2008, p. 33
- 3) Takahashi, M.: Shinnittetsu Giho. (378), 2 (2003)
- 4) Davies, G.: Materials for Automobile Bodies. Butterworth-Heinemann, 2003, p. 69
- 5) Azuma, M. et al.: Shinnittetsu Giho. (392), 45 (2012)
- 6) Senuma, T.: ISIJ Int. 52, 539 (2012)
- 7) Yang, D. Z. et al.: Metall. Trans. 16A, 1385 (1985)
- 8) Huang, J. et al.: Metall. Trans. 35A, 3363 (2004)
- 9) Azizi-Alizamini, H. et al.: Metall. Trans. 42A, 1544 (2011)
- 10) Kulakov, M. et al.: Metall. Trans. 44A, 3564 (2013)
- 11) Ogawa, T. et al.: J. Mater. Eng. Perform. 26, 3821 (2017)
- 12) Hasegawa, K. et al.: Tetsu-to-Hagané. 98, 320 (2012)
- 13) Nakada, N. et al.: Tetsu-to-Hagané. 102, 253 (2016)
- 14) Kaneko, H. et al.: Tetsu-to-Hagané. 56, 622 (1970)
- 15) Enomoto, M.: Phase Transformation of Metal. Uchida Rokakuho Publishing Co., Ltd., 2000, p. 47
- 16) Enomoto, M. et al.: Metall. Trans. 17A, 1385 (1986)
- 17) Lee, J. K. et al.: Surface Science. 256, 147 (1991)
- 18) Clemm, J. et al.: Acta Metall. 3, 70 (1955)
- 19) Aaronson, H. I. et al.: Mechanisms of Diffusional Phase Transformations in Metals and Alloys. Taylor and Francis Group, 2010, p. 49
- 20) Thermo-Calc Software AB: TCS Steels/Fe-Alloys Database Version 8.1. Thermo-Calc Software, 2016
- 21) Hillert, M.: Phase Equilibria, Phase Diagrams and Phase Transformations. Their Thermodynamic Basis. Cambridge University Press, 1998, p. 390
- 22) Nishizawa, T.: ISIJ Int. 40, 1269 (2000)
- 23) Cerda, F. M. C. et al.: Materials and Design. 116, 448 (2017)
- 24) Vlack, L. H. V.: Trans AIME. 191, 251 (1951)
- 25) Smith, C. S.: Trans AIME. 175, 15 (1948)
- 26) Azizi-Alizamini, H. et al.: Int. J. Mat. Res. 101, 534 (2010)



Shohei YABU
Sheet & Coil Research Lab.
Steel Research Laboratories
20-1 Shintomi, Futtsu City, Chiba Pref. 293-8511



Koutarou HAYASHI
Senior Researcher, PhD in Engineering
Sheet & Coil Research Lab.
Steel Research Laboratories



Toshinobu NISHIBATA
Senior Researcher
Fundamental Metallurgy Research Lab.
Advanced Technology Research Laboratories